


RESEARCH ARTICLE

Targeted regeneration and upcycling of spent graphite by defect-driven tin nucleation

Zhiheng Cheng¹ | Zhiling Luo² | Hao Zhang¹ | Wuxing Zhang¹ |
Wang Gao² | Yang Zhang³ | Long Qie¹ | Yonggang Yao¹  |
Yunhui Huang¹ | Kun Kelvin Fu⁴

¹State Key Laboratory of Materials Processing and Die & Mould Technology, School of Materials Science and Engineering, Huazhong University of Science and Technology, Wuhan, China

²Key Laboratory of Automobile Materials (Jilin University), Ministry of Education, Department of Materials Science and Engineering, Jilin University, Changchun, China

³Electronic Materials Research Laboratory (Key Lab of Education Ministry), School of Electronic and Information Engineering, and Instrumental Analysis Center, Xi'an Jiaotong University, Xi'an, China

⁴Department of Mechanical Engineering, University of Delaware, Newark, USA

Correspondence

Long Qie and Yonggang Yao, State Key Laboratory of Materials Processing and Die & Mould Technology, School of Materials Science and Engineering, Huazhong University of Science and Technology, Wuhan 430074, China.
Email: qie@hust.edu.cn and yaoyg@hust.edu.cn

Funding information

The Fundamental Research Funds for the Central Universities, HUST,
Grant/Award Number: 2021GCRC046;
The Open Fund of State Key Laboratory of New Textile Materials and Advanced Processing Technologies,
Grant/Award Number: FZ2022005;
Natural Science Foundation of Hubei Province, China, Grant/Award Number: 2022CFA031

Abstract

The recycling of spent batteries has become increasingly important owing to their wide applications, abundant raw material supply, and sustainable development. Compared with the degraded cathode, spent anode graphite often has a relatively intact structure with few defects after long cycling. Yet, most spent graphite is simply burned or discarded due to its limited value and inferior performance on using conventional recycling methods that are complex, have low efficiency, and fail in performance restoration. Herein, we propose a fast, efficient, and “intelligent” strategy to regenerate and upcycle spent graphite based on defect-driven targeted remediation. Using Sn as a nanoscale healant, we used **rapid heating (~50 ms)** to enable dynamic Sn droplets to automatically nucleate around the surface defects on the graphite upon cooling owing to strong binding to the defects (~5.84 eV/atom), thus simultaneously achieving Sn dispersion and graphite remediation. As a result, the regenerated graphite showed enhanced capacity and cycle stability (458.9 mAh g⁻¹ at 0.2 A g⁻¹ after 100 cycles), superior to those of commercial graphite. Benefiting from the self-adaption of Sn dispersion, spent graphite with different degrees of defects can be regenerated to similar structures and performance. EverBatt analysis indicates that targeted regeneration and upcycling have significantly lower energy consumption (~99% reduction)

Zhiheng Cheng, Zhiling Luo, and Hao Zhang are co-first authors.

This is an open access article under the terms of the Creative Commons Attribution License, which permits use, distribution and reproduction in any medium, provided the original work is properly cited.

© 2023 The Authors. *Carbon Energy* published by Wenzhou University and John Wiley & Sons Australia, Ltd.

and near-zero CO₂ emission, and yield much higher profit than hydro-metallurgy, which opens a new avenue for direct upcycling of spent graphite in an efficient, green, and profitable manner for sustainable battery manufacture.

KEYWORDS

battery recycling, spent graphite, targeted regeneration, upcycling graphite

1 | INTRODUCTION

With increasing attention being paid to carbon neutrality, electric vehicles (EVs) and energy storage stations are developing rapidly, which is creating significant demand for lithium-ion batteries (LIBs).^{1,2} As LIBs typically have a life span of 5–10 years, according to a report, the number of spent LIBs will be 1.08 million tons by 2023 and much more in the foreseeable future, threatening environmental stability and sustainability.^{3,4} Therefore, battery recycling is inevitable to address raw material shortage and environmental impact.⁵ Commercialized recycling methods include pyrometallurgy and hydrometallurgy, which use either high-temperature roasting or acid/alkaline leaching to recycle spent batteries, leading to severe emissions and environmental pollution. On the other hand, direct recycling has been developed recently to obtain and regenerate active battery materials without destroying them into elements, thus representing a more sustainable route as it consumes less energy and releases less waste.^{6–8}

Currently, most recycling methods focus on collecting the active materials in cathodes, while the effective recycling of graphite anodes (about 15–22 wt.% of LIBs at the cell level) is often overlooked, largely owing to their limited value and inferior performance through the use of conventional recycling methods.^{9–11} In traditional recycling, spent graphite (SG) is often burned as a reducing agent or simply discarded, thus leading to severe carbon emissions and the release of hazardous wastes.⁶ Meanwhile, the production of anode graphite consumes tremendous energy due to the requirement of ultrahigh-temperature graphitization (~3000 K, lasting for several days).^{12,13} Considering the significant amount of and huge demand for graphite in LIBs, graphite recycling is indispensable to ensure sustainable battery manufacturing and to drastically reduce the carbon footprint in anode production as well as eliminate the potential solid waste from spent batteries.

When carefully looking at the recycled materials from spent batteries, unlike cathode materials that often show large structural degradation, anode graphite typically has a relatively intact bulk structure with few defects and

impurities.^{2,14} These defects and impurities are generated during long-duration cycles, including surface defects and vacancies, binders, and solid electrolyte interphases (SEIs), which strongly influence the performance of LIBs.^{15–17} Accordingly, several measures have been adopted to regenerate SG, such as acid leaching,^{18–21} high-temperature treatment,^{22–27} and catalytic graphitization.²⁸ Nevertheless, acid and high-temperature treatment could remove SEIs and impurities of SG,²⁵ while hardly repairing structural defects like vacancies. Catalytic graphitization can deal with these structural defects, but the use of catalysts complicates the process and increases the cost. More importantly, most recycling methods are generally complex, have low efficiency, and fail in improving the performance.²⁹ As shown in Figure S1, the performance of recycled graphite is close to or at best equivalent to that of commercial graphite (CG), which is not useful in the battery market where there is a continuous demand for higher energy density.^{30,31} This capacity gap can be attributed to surface and composition defects, which can hardly be dealt with by simple calcination and wet chemistry methods.³² To minimize process complexity and potential cost, the key challenge lies in how to precisely locate the defects and achieve targeted remediation and improvement of performance in an efficient, green, and profitable manner.

Here, we report a dry, fast, and energy-efficient approach to instantaneously upcycle SG based on defect-targeted nucleation and regeneration. Sn was used as a nanoscale healant for targeted remediation due to its low melting point (231°C) along with high capacity. Using a **flash Joule heating method (e.g., 1600°C for 50 ms)**, the SnCl₂ precursor loaded on SG was thermally reduced to molten Sn, which would preferably nucleate on the defects of SG upon cooling (Figure 1A).^{33–35} The targeted Sn nucleation on defects is driven by the thermodynamically favorable binding of Sn on defects rather than graphitic carbon, as shown in Figure 1B, where the binding energy between Sn and defects is much stronger than that between Sn and graphite (5.84 vs. 0.85 eV/atom). Therefore, the surface defects act as nucleation sites that enable molten Sn dispersion and graphite

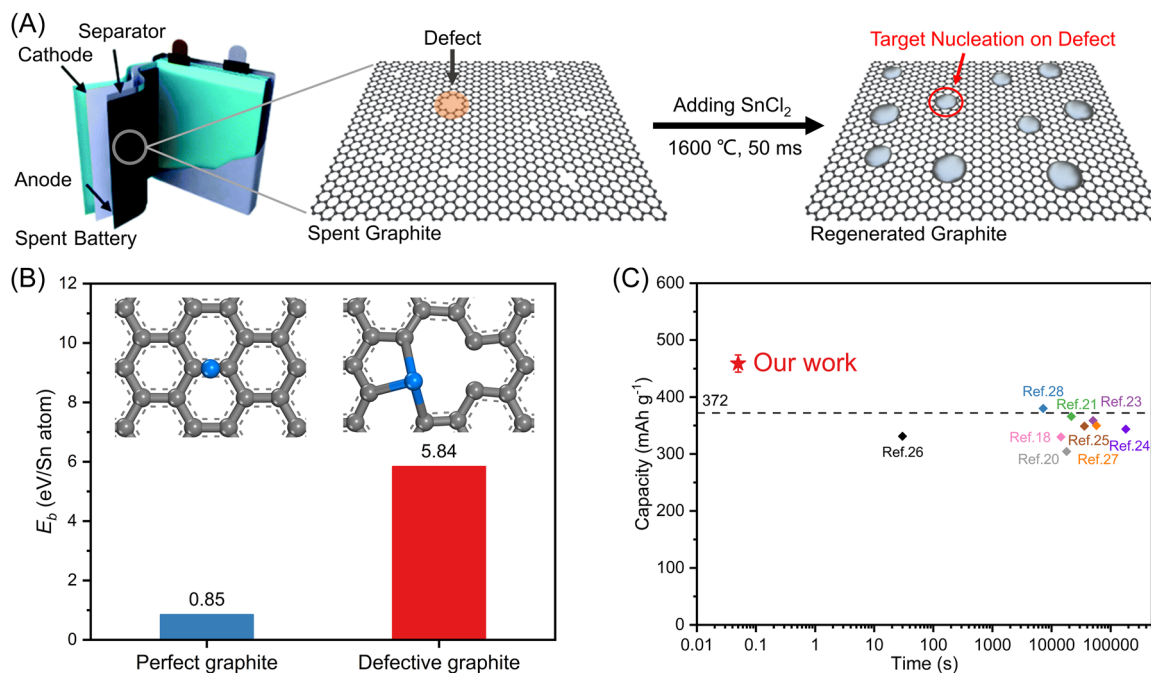


FIGURE 1 (A) Schematic of targeted regeneration and upcycling of spent graphite via **flash heating**. (B) Adsorption structures and binding energies of a single Sn atom on perfect and defective graphite. (C) Capacity and processing time of RG and those of the previously reported recycled graphite anode.

regeneration simultaneously. The flash heating not only significantly improves the energy and time efficiencies for graphite recycling but is also essential to ensuring nanoscale Sn dispersion to promote Li intercalation with improved rate and capacity. As a result, the regenerated graphite (RG) delivered a capacity of 458.9 mAh g^{-1} at 0.2 A g^{-1} after 100 cycles, which is much higher than those of the CG and other recycled graphite (Figure 1C). Taking the complex state of SG into consideration, we test the performance of RG from different SG, which are similar owing to the self-adaption of Sn dispersion. This work, therefore, provides a route to effectively regenerate and upcycle SG in a very rapid manner to achieve superior electrochemical performances, thus realizing efficient, green, and profitable recycling of the often-discarded graphite for sustainable energy applications.

2 | RESULT AND DISCUSSION

To compare the structural evolution and potential defects of graphite after long-term cycling, we first characterized the structure of CG and SG in detail. X-ray diffraction (XRD; Figure 2A) was performed to determine the bulk structure, where both patterns match well with that of graphite (JCPDS No. 1-640) without any impure peaks, indicating that SG mostly retained an intact layer structure after long-term cycling.³⁶ Further, the scanning

electron microscopy (SEM; Figure 2B) image shows that the surface of CG is smooth and flat, while the high-resolution transmission electron microscopy image (HRTEM; Figure 2C) clearly shows an array of carbon atoms arranged regularly with a lattice fringe spacing of 0.34 nm , corresponding to the (002) facet of graphite.³⁷

Meanwhile, the degrees of graphitization of these samples were characterized by Raman spectroscopy. As shown in Figure 2D, the peaks at 1340 and 1580 cm^{-1} are attributed, respectively, to the vibration modes of disordered graphite (D band) and crystalline graphite (G band).³⁸ Compared with $I_D/I_G = 0.079$ for CG, SG shows a much higher D peak and correspondingly increased D/G ratio of $I_D/I_G = 0.797$, indicating that SG has much more disordered or defective carbon bonds than CG on the surface after charging/discharging processes, despite its relatively intact bulk layered structure. Microscopically, the surface of SG is rough and many edges and exfoliated graphite layers exist because of long-term cycling and faulty intercalation, as shown in Figure 2E. The HRTEM images (Figure 2F) of SG also demonstrate a much higher degree of disorder, clearly showing the lattice fringe. More importantly, there are many atomic vacancies on the surface of SG, which clearly indicates the destruction of the graphite surface, particularly at the nanoscale.

The elemental mapping (Figure S2) shows that SG is composed of carbon, oxygen, fluorine, and phosphorus,

and Table S1 shows their contents. These elements arise from surface oxidation, residual electrolytes (LiPF_6), and SEI.³⁹ The existence of these impurities was further confirmed by thermogravimetric analysis (TGA, Figure S3) and a Fourier-transform infrared spectrometer (FT-IR, Figure S4). The above characterizations indicate that compared with CG, SG shows a relatively intact bulk structure but with abundant surface defects and impurities after cycling, which requires proper remediation to restore its structure and capacity.

The structural defects of SG, such as the above-mentioned graphite layer peeling and carbon atom vacancies, are usually repaired through carbon coating or re-graphitization under high temperatures for regeneration.^{23,40} However, these processes require a new surface or new graphitization, which are not only time- and energy-consuming but also require delicate coating techniques, and are thus not ideal for efficient and profitable SG recycling. Considering the physico-chemical differences between defects and the carbon/graphite layer, defect-targeted regeneration is possible and much more economical. In particular, carbon defects could act as nucleation sites to trap metal nanoparticles.^{34,41,42} Therefore, we chose Sn, a metal with a low melting point and a high theoretical capacity of 993 mAh g^{-1} , as a candidate to achieve energy-efficiency targeted regeneration.

Theoretical analysis was first used to reveal the possibility of targeted regeneration by defect-driven Sn nucleation. We used density functional theory (DFT) methods to study the nucleation and growth of melting Sn on perfect and defective graphene using the Perdew–Burke–Ernzerhof (PBE) exchange–correlation functional.^{43,44} Since the adsorption of Sn atoms mainly occurs on the top layer of graphite, we adopted graphene with vacancies to represent the defective graphite. The vacancies are created by removing x carbon atoms ($\text{D}_x, x \leq 4$, Figure S5). Although small-size vacancy structures, such as locally relaxed vacancy structures have a stronger adsorption effect on the transition-metal clusters.^{45,46} Compared with the fully optimized ground-state structures, the locally optimized structures have higher energy and thus stronger bonding with metal clusters. We adopted the binding energy (E_b) and the adsorption energy (E_{ad}) to measure the bonding strength of Sn atoms and Sn clusters on graphene, respectively. E_b includes C–Sn and Sn–Sn interactions, while E_{ad} only includes C–Sn interactions (details of the calculation are presented in the Supporting Information). These two parameters were used not only to separate the complex C–Sn and Sn–Sn interactions but also to quantify the adsorption and growth behavior of Sn clusters on various graphene substrates.

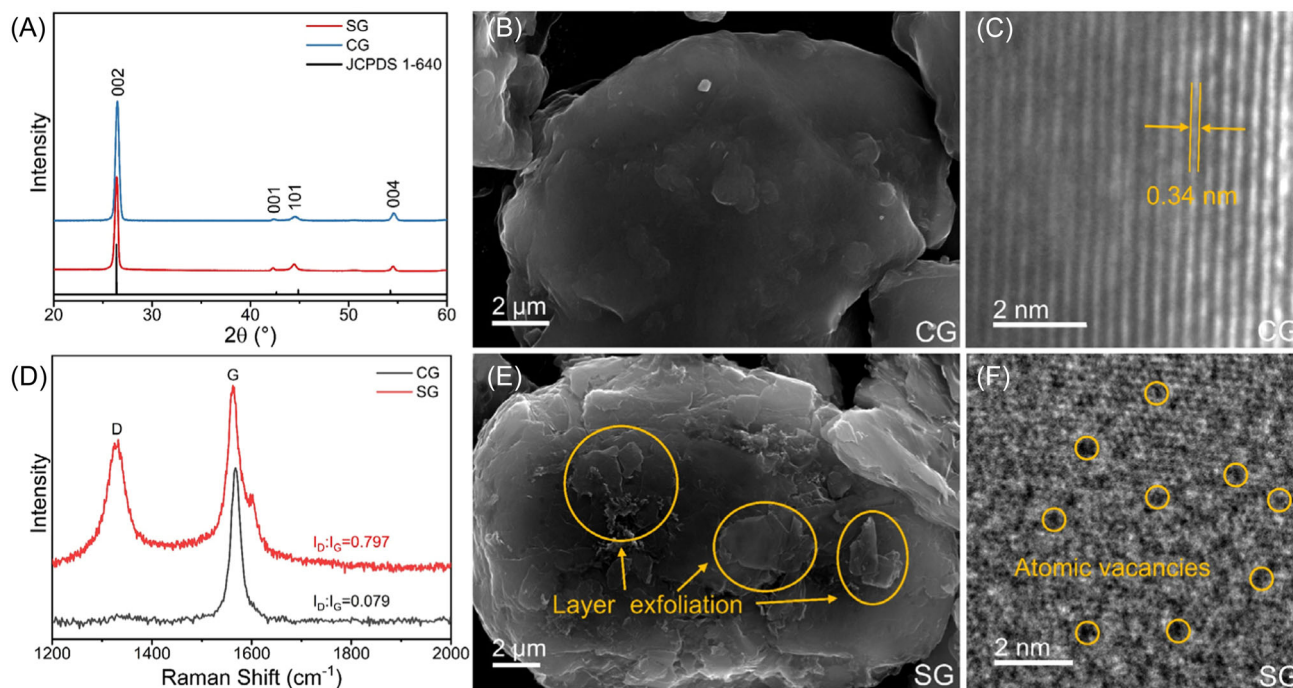


FIGURE 2 Structural changes of SG compared with CG. (A) XRD patterns of CG and SG. The inset shows the magnified view of (002) peaks. (B) SEM images and (C) TEM images of CG. (D) Raman spectra of CG and SG. (E) SEM and (F) TEM images of SG.

In Figure 3A, E_b of a single Sn atom binding on defective graphene, ranging from 2.95 to 5.84 eV for different configurations, is significantly greater than that on perfect graphene (0.85 eV), which indicates that Sn atoms easily adsorb and nucleate on the vacancies of graphene. The smaller E_b of Sn atoms on perfect graphene mainly arises from the attraction between Sn atoms and the π -system of graphene. Notably, E_b of a single Sn atom at different adsorption sites on perfect graphene has a range of 0.61–0.85 eV (Figure S6). The small diffusivity barrier (~ 0.24 eV) is favorable for the rapid migration of individual Sn atoms, which promotes the saturation of vacancies and the growth of Sn clusters. In contrast, the larger E_b of Sn atoms on defective graphene mainly originates from the covalent binding between Sn atoms and the dangling C atoms at vacancies. In addition, the decrease of E_b on defective graphene with increasing number of Sn atoms indicates that Sn–C covalent bonding is more favorable than Sn–Sn bonding (Figure S7A). Therefore, the individual Sn atoms preferentially bond to dangling C atoms at vacancies

rather than bonding with Sn clusters, which facilitates the rapid repair of vacancy defects and Sn dispersion. On the other hand, E_{ad} of Sn clusters on defective graphene gradually decreases with increasing number of Sn atoms (Figure S7B). Taking the D₃ substrate as an example (Figure 3B), E_{ad} is maximum when two Sn atoms are adsorbed, and in this case, all the dangling C atoms at the vacancy are saturated. As the number of Sn atoms further increases, the gradually decreasing E_{ad} hinders further growth of Sn clusters. This stems from the large atomic radius of Sn atoms, which makes it difficult for Sn clusters to form stable cluster structures at vacancies. These results suggest that Sn atoms preferentially saturate the dangling C atoms at vacancies and eventually form small Sn nanoclusters on defective graphene, demonstrating that the melting Sn can efficiently heal the defect of graphite.

To experimentally confirm the above results, we further used CG and needle coke, a precursor of CG with many surface defects (Figure S8), to confirm defect-driven Sn nucleation and dispersion. After loading with

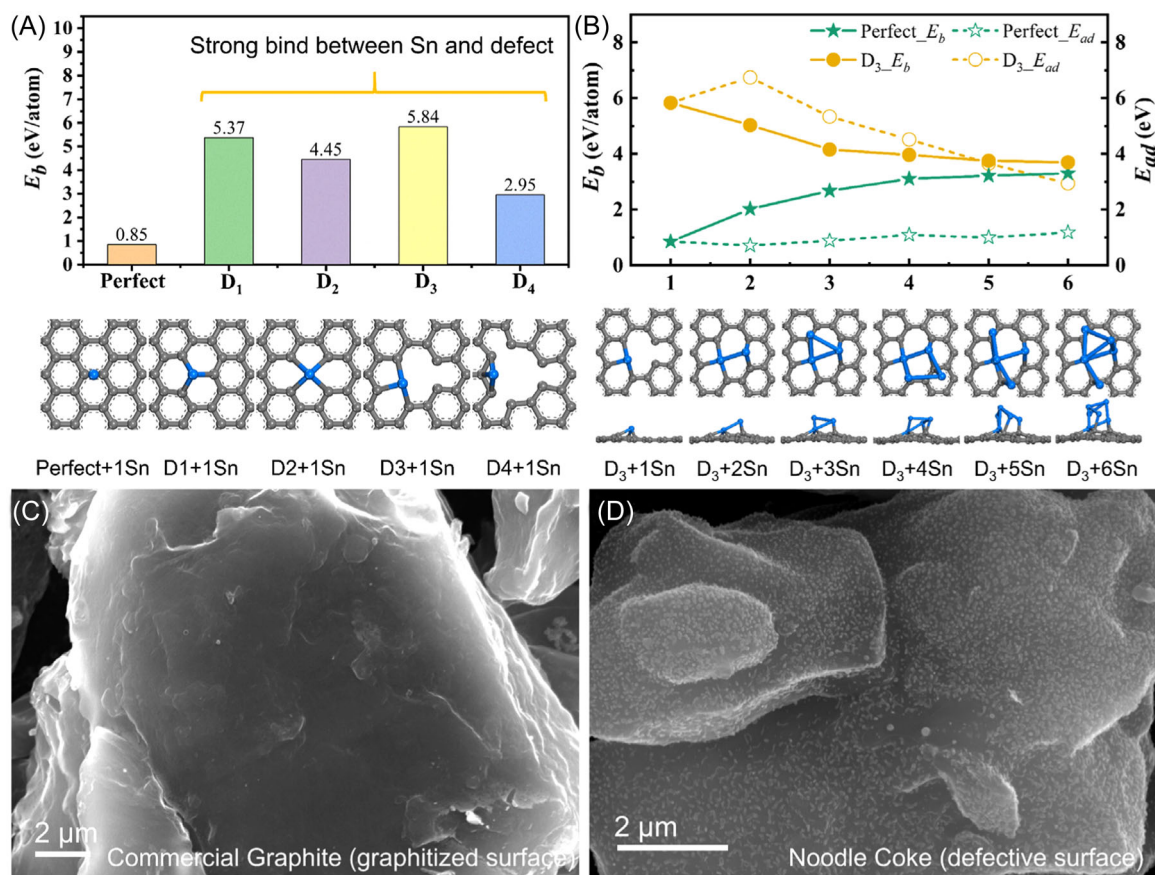


FIGURE 3 Theoretical and experimental proof of targeted remediation. (A) Binding energy (E_b in eV/Sn atom) for the single Sn atom on perfect and defective graphene substrates (D₁–D₄). (B) Binding energy (E_b in eV/Sn atom) and adsorption energy (E_{ad} in eV) of Sn_n clusters on different graphene substrates and the adsorption structures on the D₃ substrate. SEM images of (C) CG and (D) needle coke after nucleation.

SnCl_2 , both samples were heated to 1600°C within 50 ms by Joule heating. As shown in the SEM images (Figure 3C), Sn particles can hardly be found on the surface of CG because of its graphitized surface with fewer defects. However, for needle coke, we can see numerous nanoparticles evenly distributed on its surface (Figure 3D), owing to the nature of the defective surface, which effectively disperses and anchors the molten Sn.⁴¹ Therefore, the above theoretical and experimental work proves the feasibility of the targeted regeneration of SG via defect-driven Sn nucleation.

To investigate the regeneration of actual SG, we explored different loading and flash heating parameters to regulate the microstructure of Sn dispersion, particularly the particle size and associated electrochemical properties.^{47,48} Four mass fractions of Sn in SG (0.5%, 1%, 2%, and 5%, arising from SnCl_2) and several heating temperatures (1400°C , 1600°C , and 1800°C , all for 50 ms) were chosen. Figure S9 provides the temperature profiles of different peak temperatures. For all the profiles, the temperature reached the maximum

value in 50 ms at a heating rate of $\sim 10^4$ K/s and then decreased at a cooling rate of $\sim 10^3$ K/s. Such a high temperature not only thermally reduces SnCl_2 to Sn but also turns it into a molten and dynamic state to enable the targeted location of defects.⁴⁹

Figures 4A,B and S10 show the SEM images of RG with the different loadings. If we increase the loading, the particle size will be bigger. When we increased the loading to 5%, micrometer-sized Sn particles were found. When we set the mass fraction at 1%, the number and diameter of Sn particles visibly decreased as the heating temperature increased due to the increasing vapor pressure (Figure S11). The vapor pressure is 12.7 Pa when the temperature is 1400°C , but it rapidly increases to 121 Pa for 1600°C and 745 Pa for 1800°C (Figure S12). Such a high saturated vapor pressure causes evaporation of melting Sn and leads to few nanoparticles.³⁵ Overall, uniform dispersion of Sn nanoparticles could be achieved under the optimal condition of 1% Sn loading content and 1600°C flash heating, which could induce a good balance between defect healing and Sn particle size.

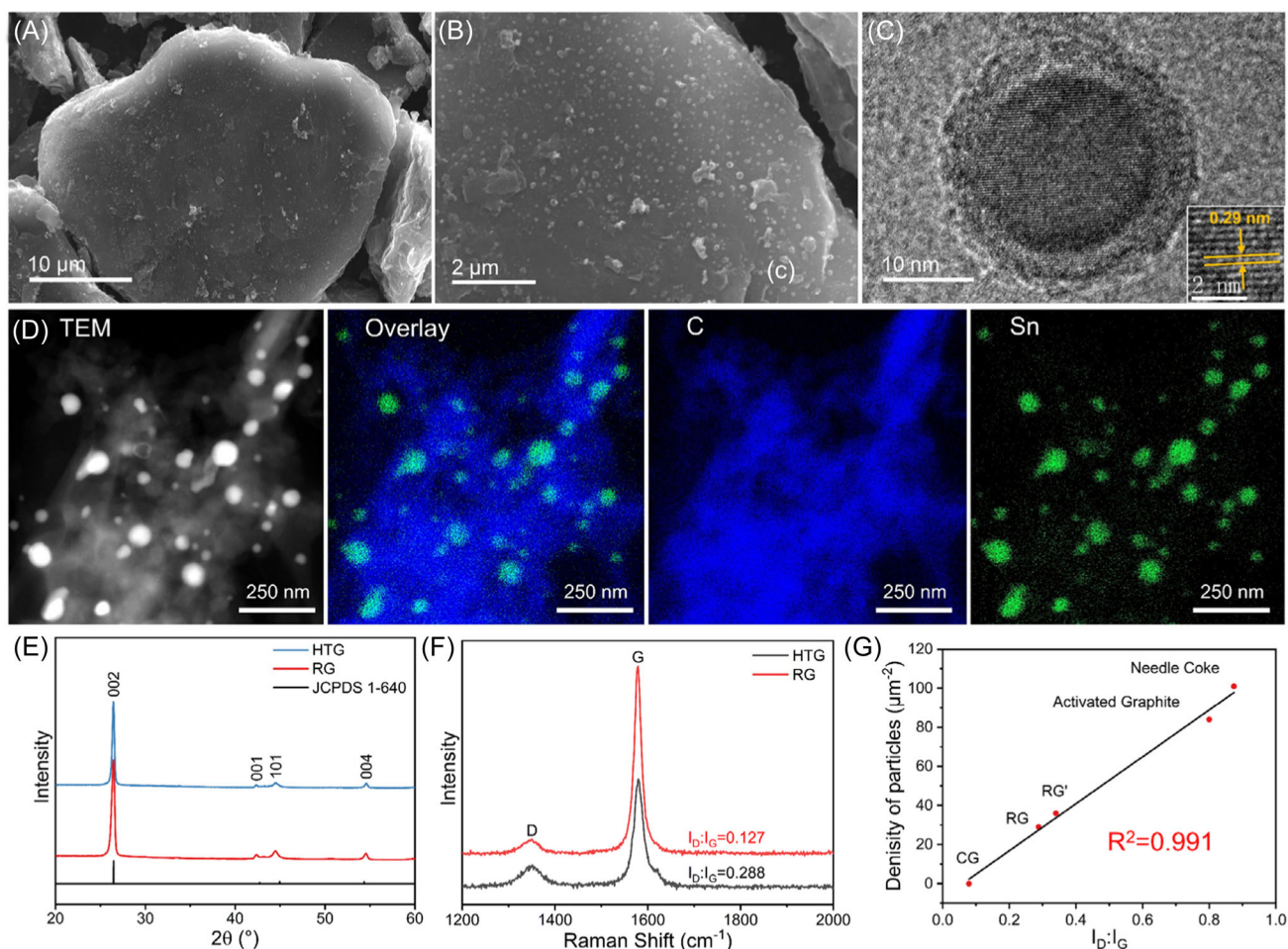


FIGURE 4 (A, B) SEM images of RG. (C) TEM image of RG. (D) Elemental mapping of RG. (E) XRD patterns and (F) Raman spectra of HTG and RG. (G) Sn particle density of CG, RG, RG', activated graphite, and needle coke as a function of I_D/I_G .

Furthermore, we characterized the composition and elemental distribution of RG by X-ray photoelectron spectroscopy (XPS; Figure S13). Remarkably, the spectra of C 1s are deconvoluted into three peaks, which can be assigned to C–O (285.3 eV), C–C (284.8 eV), and C–Sn (284.1 eV).⁵⁰ This indicates the direct bonding between C and Sn, which also coincides with the result of DFT analysis. The HRTEM (Figure 4C) image showed good crystallization of Sn nanoparticles, and the Sn nanoparticle has a core-shell structure. The regular lattice fringes with lighter colors belong to graphite. The interplanar spacing of the darker particle is 0.29 nm, corresponding to the (200) facet of Sn. The crystal structure of Sn (JCPDS No. 86-2265) could also be confirmed in the inverse fast Fourier transformation (Figure S14). Elemental mapping (Figure 4D) indicated an enrichment of Sn in nanoparticles, demonstrating uniform decoration of Sn nanoparticles. Notably, in the line scan of EDS (Figure S15), the signal of O is high related to that of Sn, indicating that the shell is SnO₂. Compared with Sn metal, SnO₂ performs better in the cycling test due to the generation of Li₂O during the first cycling.^{51,52} This offers a strong framework to relieve the stress of alloying and plays a better role as a healant.⁴⁸ Besides, Li₂O may consume the limited Li in the battery. However, when we take the low loading of Sn into account, the consumption of Li is negligible.

We also accurately measured the loading weight of Sn in RG by inductively coupled plasma-optical emission spectrometry (ICP-OES), which shows that the weight percent of Sn is 0.48% (Table S2). The loading mass of Sn is less than 1% due to its evaporation during the high-temperature heating process. FT-IR was performed to investigate the residual organics after high-temperature rapid pyrolysis (Figure S16). The peaks of the organic function group disappear or decline dramatically, which indicates complete carbonization of binders.

Noticeably, except for Sn loading, the performance of graphite could also be affected by high-temperature treatment. Therefore, SG with the same heating treatment but without the addition of Sn (named HTG) was prepared as a comparison. XRD profiles of RG and HTG (Figure 4E) accurately fit with the peaks of graphite (JCPDS No. 1-640), indicating a good bulk layered structure. However, a small shift of the (002) peak can be found in them, indicating the defects present within. These internal defects cannot be healed owing to the low temperature and limited time, but they play a major role in the transfer of Li ions and offer more sites to absorb Li ions.^{53–57} In addition, we note that there is no peak in the XRD pattern belonging to Sn, which could be explained by the low content of Sn. The Raman spectrum (Figure 4F) shows the degree of disorder on the surface

of graphite. The heating process has positive effects in removing the surface defects as the I_D/I_G decreases from 0.797 for SG to 0.288 for HTG. Importantly, the ratio was further reduced to 0.127 with the addition of Sn, which confirms that adding Sn could reduce surface defects due to the targeted nucleation of Sn particles in defects. In Figure 4G, we summarize the statistics of the density of Sn particles on CG, RG, and regenerated needle coke to analyze its correlation with surface defects, which were characterized by I_D/I_G . Notably, they show a strong linear correlation with a linearity of 0.998, which directly indicates the strong corresponding relation between Sn particles and the defects and supports the defect-driven nucleation of Sn. Moreover, SG with an I_D/I_G of 0.34 (named RG') and graphite activated by CO₂ with an I_D/I_G of 0.80 were chosen to confirm the linear correlation, and the data were still strongly correlated. This linear correlation indicates the self-adapting regeneration of SG, as graphite with different degrees of defects could be regenerated with the loading of 1% by adjusting the size of their Sn particles.

The electrochemical performance of RG, HTG, and CG was first evaluated using half-cells and is shown in Figure 5. Cyclic voltammetry curves (CVs) of RG (Figure 5A) were first carried out to analyze its electrochemical behavior. The cathode reduction peak at 0.58 V during the first charge process is attributed to the generation of SEI on the graphite surface. Importantly, the disappearance of the reduction peak during the subsequent scans means that no new SEI formed, indicating the good structure stability of RG. The oxidation peaks at around 0.33 V correspond to the deintercalation of Li⁺ in graphite.⁵⁸ Besides, no obvious oxidation and reduction peaks belonged to Sn at 0.4–0.8 V, indicating that nanoscale Sn makes no obvious contribution to the capacity due to its neglectable loading weight.⁵⁹

In the long-term cycling test (Figure 5B), the RG retained outstanding cycling stability, showing a reversible discharge capacity of 458.9 mAh g^{−1} after 100 cycles at a current density of 0.2 A g^{−1}, which is much higher than those of HTG (380.5 mAh g^{−1}) and CG (377.4 mAh g^{−1}). It was confirmed that the RG electrode could retain electrochemical cycling stability, which is strongly linked to the nanosized Sn and the flexible conductive buffer of graphite. Besides, as shown in Figure S17, for RG from different spent batteries, the capacity just increases by 104.3% when there is approximately a 200% increase in I_D/I_G , indicating that the degree of defects does not influence the electrochemical performance strongly. According to the performance of activated graphite, we can use CO₂ activation to further improve the consistency of RG in practical applications. We also test the cycling

performance of RG with a loading of 0.2%, 2%, and 5% to determine how the dispersion and loading of Sn affect the electrochemical properties. Figure S18 shows their cycling performance. Low loading of 0.2% leads to unsatisfactory capacity (388.7 mAh/g) like HTG, because numerous defects could not be repaired by limited Sn. With a high loading of 2%, RG with a high Sn loading of 2% shows a similar capacity (454.8 mAh/g) as RG with the Sn loading of 1%, indicating that target regeneration remains effective in a certain loading range. However, when we increase the loading to 5%, its capacity is much higher than that of RG but decreases fast, resulting in worse performance than RG. As Sn is a high-capacity anode material with poor cycling stability, such high loading inevitably weakens the cycling stability.

As for the rate test (Figure 5C), RG also shows a capacity of 429.6, 402.3, 357.8, and 256.0 mAh g⁻¹ at a current density of 0.1, 0.2, 0.5, and 1 A g⁻¹, respectively, which demonstrates better rates than that of CG. When the

density returned to 0.1 A g⁻¹, a capacity of 424.3 mAh g⁻¹ could be obtained. The better rate performance could be attributed to two reasons. On the one hand, there were abundant (Sn-covered) surface edges and defects, which shortened the transport length of Li⁺ compared with the long distance in planar intercalation, thus promoting the rapid intercalation and de-intercalation of Li⁺ in graphite and rate performances.⁶⁰ On the other hand, Sn particles could enable efficient Li-ion transfer into graphite layers, as their high Li binding energy and Li⁺ conductivity guide Li ions into the surface defects of graphite.⁶¹

Electrochemical impedance spectroscopy (EIS) was performed to determine the kinetic properties. In Figure 5D, the semicircle in the high-frequency region relates to the charge-transfer resistance and the line in the medium-low frequency region shows the Warburg impedance (Z_w) corresponding to the ion-diffusion resistance.⁶² Table S3 shows the simulative results of EIS. The small resistance of 44.7 Ω of RG is due to

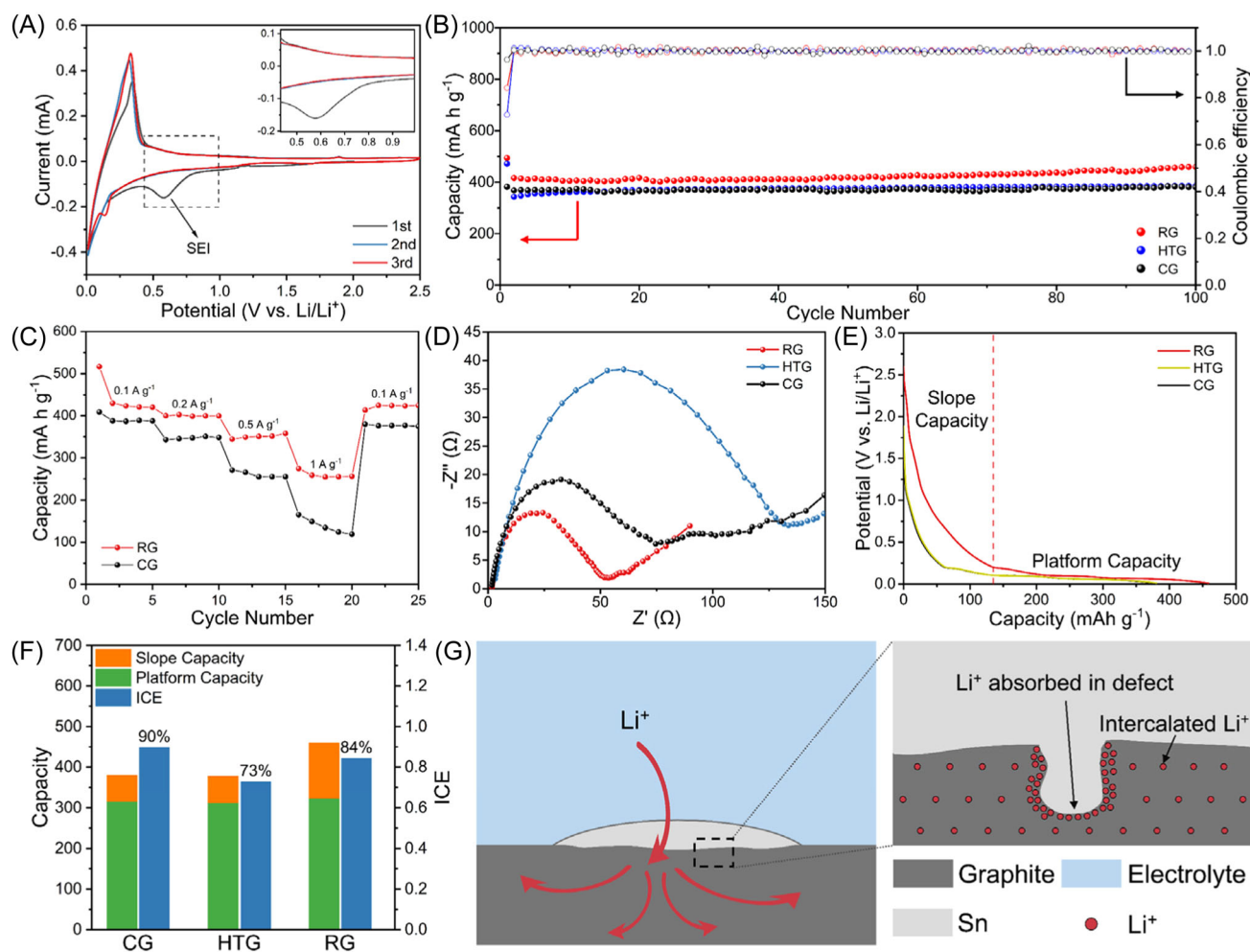


FIGURE 5 Electrochemical performance of RG, HTG, and CG. (A) CV curve of RG. (B) Cycling performance at a current density of 0.2 A g⁻¹. (C) Rate performance of RG and CG. (D) Electrochemical impedance spectra. (E) Discharge curves at the 100th cycle. (F) Capacity distribution and initial Coulombic efficiency (ICE). (G) Schematic representation of lithium intercalation in RG.

enhanced cycling and ion transport abilities as compared with HTG (127.1 Ω) and CG (73.5 Ω), which benefited from the extra Li^+ transfer channel and better conductivity of Sn metal. To further understand the Li^+ diffusion kinetics of RG at different lithiation/de-lithiation stages, galvanostatic intermittent titration technique (GITT; Figure S19A) profiles and the Li^+ diffusion coefficient (D_{Li^+} ; Figure S19B) were determined. RG shows a higher D_{Li^+} than CG at different lithiation/de-lithiation stages due to the abundant edges and defects in RG.

To reveal the origin of enhanced electrochemical performance, we further analyzed the discharge curves of HTG, CG, and RG at the 100th cycle (Figure 5E). For a typical curve of graphite, also known as the “Card House” model, the capacity can be divided into two parts, the slope capacity and the platform capacity, where the slope of the discharge curve represents the process with a wide energy distribution such as adsorption on graphite edges or defects, and the voltage plateau could be derived from the intercalation of Li^+ into graphitic layers.^{63,64} As shown in Figure 5F and Table S4, the platform capacity of RG (323.5 mAh g^{-1}) is close to those of CG (312.3 mAh g^{-1}) and HTG (315.7 mAh g^{-1}), indicating a similar intact bulk structure that determined the number of intercalating Li^+ . In contrast, the slope capacity of RG (135.2 mAh g^{-1}) was much higher than those of CG (65.1 mAh g^{-1}) and HTG

(64.8 mAh g^{-1}), revealing the great contribution of absorbed Li^+ to capacity. Furthermore, we use the differential capacity curve (Figure S20) to analyze the difference of capacity between them. The curves of RG and HTG are similar under 0.25 V, indicating the same insertion reaction of Li ions and the generation of LiC_6 .⁶⁰ In contrast, in the range of 0.25–2.5 V, the range of absorbed Li ions and the dQ/dV of RG are much higher than those of HTG, confirming the impact of surface defects protected by Sn particles. Besides, the ICE (84.3%) of RG is much higher than that of HTG (72.8%) and approaching that of CG (89.7%), which can be attributed to the targeted remediation of surface defects.^{65–67} Figure 5G further illustrates the schematic of Li^+ transfer and storage in RG. Due to the protected surface defects, Li^+ could diffuse into graphite through them rapidly, with some Li^+ absorbed on defects, thus showing a higher rate and enhanced capacity. Besides, the nanoscale Sn supported by graphitic carbon can decrease the stress during cycling, resulting in better cycling stability.⁶⁶

As discussed in the introduction, the recycling of SG should be more profitable, which can be achieved by a simplified process or less input of materials and energy. Hydrometallurgy can obtain graphite products, but involves multiple time-consuming chemical processes and a huge amount of wastewater. In contrast, as shown in Figure 6A, our targeted regeneration method could

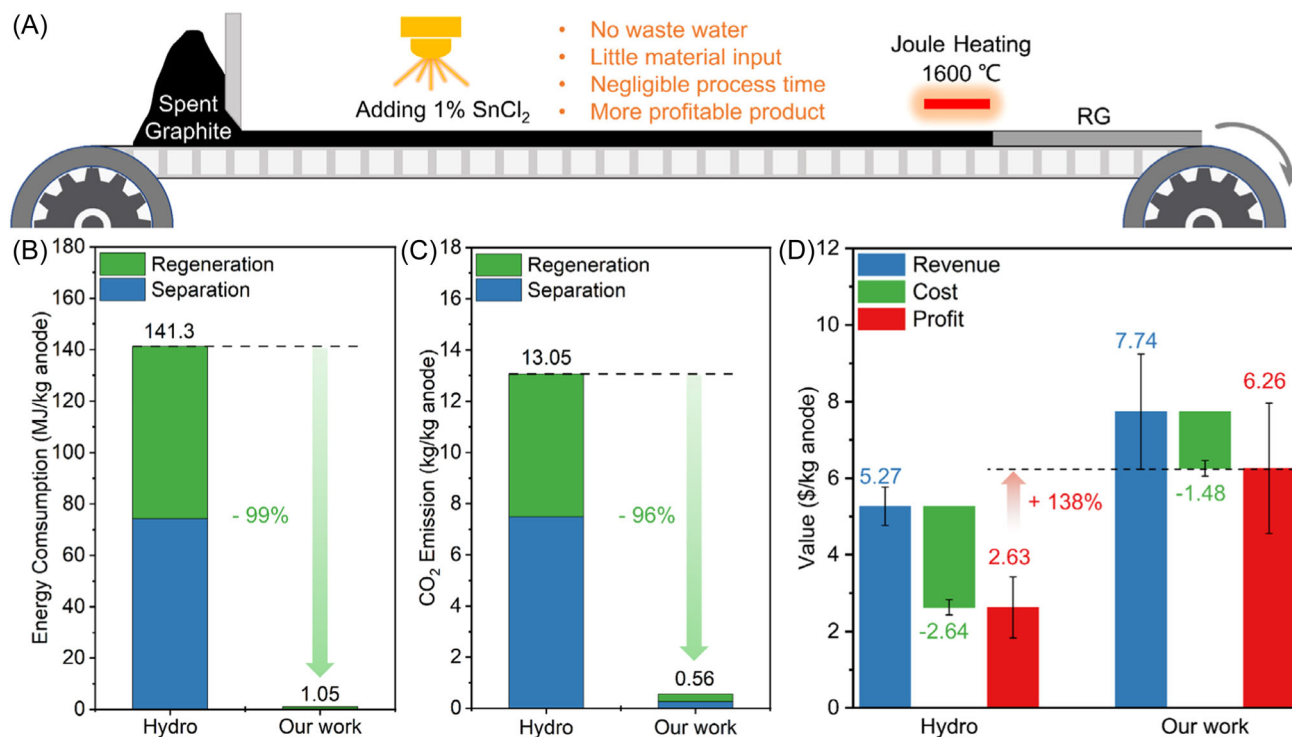


FIGURE 6 Economic and environmental analyses of different recycling methods. (A) Illustrations of spent graphite upcycle by the targeted regeneration method with roll-to-roll scalability. EverBatt analysis of (B) the total energy consumption, (C) the CO_2 emission, and (D) the cost and profit of anode recycling, by comparing hydrometallurgy and our targeted regeneration methods.

obtain RG by using simple roll-to-roll equipment as in our past work.⁶⁸ Before regeneration, the residue lithium in SG could be extracted through a process flow including acid leaching, purification, and precipitation from recycled graphite powders, as shown in Figure S21, which further increases profit and does not affect the graphite structure and the subsequent regeneration.^{69–71} SG was released into a conveyor with a belt speed of 12 m/min and a scraper was used to achieved suitable density. Then, SG was sprinkled with a SnCl₂ ethanol-based solution and placed in a heater to obtain RG. This process can save considerable time and energy, and yield efficient materials, with little waste emissions.

Furthermore, to quantify the economic and environmental impacts, we used the EverBatt model developed by the Argonne National Laboratory to assess the entire recycling and regeneration process for our method and hydrometallurgical recycling. First, both recycling methods were divided into separation and regeneration. Specifically, the energy consumption of the targeted regeneration is 1.05 MJ/kg anode in Figure 6B (0.304 MJ/kg anode for separation and 0.748 MJ/kg anode for regeneration), which is much lower than that obtained using the hydrometallurgical process (74.3 MJ/kg anode for separation and 67.0 MJ/kg anode for regeneration). The technological parameters of the targeted regeneration are shown in Table S5 after energy and environmental analyses. The same tendency is found for the emission of carbon dioxide (Figure 6C). Targeted regeneration has much lower emission (0.26 kg/kg anode for separation and 0.30 kg/kg anode for regeneration), only 4.29% of that of hydrometallurgy, which indicates that targeted regeneration has a much lower carbon footprint. Besides, other wastes are estimated, such as toxic gas and wastewater. For targeted regeneration, Cl₂ is produced during the reduction of SnCl₂, and its weight is about 8.95×10^{-4} kg/kg battery. Compared with the 10^{-1} – 10^{-2} kg/kg battery waste gas emission of pyrometallurgy and the 10^1 – 10^2 kg/kg battery wastewater of hydrometallurgy, it is clear that our target regeneration is more environmentally friendly.⁷² In addition, Table S6 lists the toxic chemical agents used in hydrometallurgy, such as sulfuric acid, hydrogen peroxide, hydrochloric acid, soda ash, and sodium hydroxide.

The cost and potential profit of the two recycling and regeneration methods are also carefully compared (Figure 6D). As shown in Figure S22, the costs depend on the materials, labor, utilities, other direct costs, battery disassembly, depreciation, other fixed cost, and regeneration. Besides, Figures S23 and S24 provide detailed data about the revenue analysis, such as recycling efficiency, the trading value, and the total revenue. The cost of hydrometallurgical recycling

reaches 2.64 \$/kg anode, while this is only 1.48 \$/kg anode for targeted regeneration. The cost saving could be attributed to the use of much fewer materials and less energy input. Based on the difference between the cost and revenue, the potential profits of different recycling methods could be determined. Targeted regeneration yields a much higher profit of 6.26 \$/kg anode because of (1) low cost (it involves the use of fewer materials and lower energy in the entire recycling process) and (2) valuable product (the higher capacity of RG than that of CG leads to more revenue). It thus yields at least twofold more profit than hydrometallurgical methods. In general, targeted regeneration makes graphite recycling not only profitable and economical but also much more sustainable and environmentally friendly.

3 | CONCLUSION

In this work, we propose an efficient, energy-saving, and dry recycling method to regenerate and upcycle SG through targeted defect remediation. The theoretical calculation reveals that surface defects of SG have a strong attraction to the nucleation of Sn, which makes targeted regeneration possible. In this way, flash Joule heating was used to decompose the precursor and enable Sn dispersion and graphite regeneration accurately. Due to the appropriate size of Sn particles and the maintained lithium-storage activity of regenerated defects, the RG containing negligible Sn showed an ICE of 84.3% and an enhanced capacity of 458.9 mAh g⁻¹ after 100 cycles. Owing to the self-adaptation of Sn nucleation, different SGs perform similarly in the cycling test, indicating the limited effect of mixing different graphite. Moreover, environmental and economic impacts analyzed by EverBatt indicate that our method requires the least energy and material input, generates the least CO₂, and has the highest profit compared with traditional hydrometallurgical recycling. The targeted regeneration and upcycling method, therefore, demonstrates ultrahigh energy and time efficiency, which could provide a new pathway for the direct recycling of SG and more sustainable battery applications.

ACKNOWLEDGMENTS

Y. Yao was supported by the Natural Science Foundation of Hubei Province, China (Grant No. 2022CFA031), the Open Fund of State Key Laboratory of New Textile Materials and Advanced Processing Technologies (FZ2022005), and the Fundamental Research Funds for the Central Universities, HUST: 2021GCRC046. We acknowledge the support of the Analytical and Testing Center, Huazhong University of Science and Technology,

and the support of the Instrument Analysis Center, Xi'an Jiaotong University.

CONFLICT OF INTEREST STATEMENT

The authors declare that there are no conflict of interests.

ORCID

Yonggang Yao  <http://orcid.org/0000-0002-9191-2982>

REFERENCES

- Goodenough JB. Electrochemical energy storage in a sustainable modern society. *Energy Environ Sci.* 2014;7(1):14-18.
- Fan E, Li L, Wang Z, et al. Sustainable recycling technology for Li-ion batteries and beyond: challenges and future prospects. *Chem Rev.* 2020;120(14):7020-7063.
- Ciez RE, Whitacre JF. Examining different recycling processes for lithium-ion batteries. *Nat Sustain.* 2019;2(2):148-156.
- Zhao Y, Kang Y, Fan M, et al. Precise separation of spent lithium-ion cells in water without discharging for recycling. *Energy Storage Mater.* 2022;45:1092-1099.
- Baars J, Domenech T, Bleischwitz R, Melin HE, Heidrich O. Circular economy strategies for electric vehicle batteries reduce reliance on raw materials. *Nat Sustain.* 2021;4(1):71-79.
- Abdollahifar M, Doose S, Cavers H, Kwade A. Graphite recycling from end-of-life lithium-ion batteries: processes and applications. *Adv Mater Technol.* 2023;8(2):2200368.
- Wang T, Song Z, Zhang Y, et al. Direct recycling of shorted solid-state electrolytes enabled by targeted recovery. *Energy Stor Mater.* 2022;52:365-370.
- Barbhuiya NH, Kumar A, Singh A, et al. The future of flash graphene for the sustainable management of solid waste. *ACS Nano.* 2021;15(10):15461-15470.
- Wang J, Liang Z, Zhao Y, et al. Direct conversion of degraded LiCoO₂ cathode materials into high-performance LiCoO₂: a closed-loop green recycling strategy for spent lithium-ion batteries. *Energy Storage Mater.* 2022;45:768-776.
- Li L, Fan E, Guan Y, et al. Sustainable recovery of cathode materials from spent lithium-ion batteries using lactic acid leaching system. *ACS Sustainable Chem Eng.* 2017;5(6):5224-5233.
- Natarajan S, Aravindan V. An urgent call to spent LIB recycling: whys and wherefores for graphite recovery. *Adv Energy Mater.* 2020;10(37):2002238.
- Dreimol CH, Guo H, Ritter M, et al. Sustainable wood electronics by iron-catalyzed laser-induced graphitization for large-scale applications. *Nat Commun.* 2022;13:3680.
- Saadi MASR, Advincula PA, Thakur MSH, et al. Sustainable valorization of asphaltene via flash joule heating. *Sci Adv.* 2022;8(46):eadd3555.
- Liu J, Shi H, Hu X, et al. Critical strategies for recycling process of graphite from spent lithium-ion batteries: a review. *Sci Total Environ.* 2021;816:151621.
- Liu X, Yin L, Ren D, et al. In situ observation of thermal-driven degradation and safety concerns of lithiated graphite anode. *Nat Commun.* 2021;12:4235.
- Ding Y, Qiao ZA. Carbon surface chemistry: new insight into the old story. *Adv Mater.* 2022;34(42):2206025.
- Wandt J, Jakes P, Granwehr J, Eichel R-A, Gasteiger HA. Quantitative and time-resolved detection of lithium plating on graphite anodes in lithium ion batteries. *Mater Today.* 2018;21(3):231-240.
- Yang J, Fan E, Lin J, et al. Recovery and reuse of anode graphite from spent lithium-ion batteries via citric acid leaching. *ACS Appl Energy Mater.* 2021;4(6):6261-6268.
- Xu C, Ma G, Yang W, et al. One-step reconstruction of acid treated spent graphite for high capacity and fast charging lithium-ion batteries. *Electrochim Acta.* 2022;415:140198.
- Zhang Z, Zhu X, Hou H, Tang L, Xiao J, Zhong Q. Regeneration and utilization of graphite from the spent lithium-ion batteries by modified low-temperature sulfuric acid roasting. *Waste Manage.* 2022;150:30-38.
- Alcaraz L, Díaz-Guerra C, Calbet J, López ML, López FA. Obtaining and characterization of highly crystalline recycled graphites from different types of spent batteries. *Materials.* 2022;15(9):3246.
- Gao Y, Wang C, Zhang J, et al. Graphite recycling from the spent lithium-ion batteries by sulfuric acid curing-leaching combined with high-temperature calcination. *ACS Sustainable Chem Eng.* 2020;8(25):9447-9455.
- Gao Y, Zhang J, Jin H, et al. Regenerating spent graphite from scrapped lithium-ion battery by high-temperature treatment. *Carbon.* 2022;189:493-502.
- Fan E, Lin J, Zhang X, et al. Anode materials sustainable recycling from spent lithium-ion batteries: an edge-selectively nitrogen-repaired graphene nanoplatelets. *eTransportation.* 2022;14:100205.
- Dong S, Song Y, Ye K, et al. Ultra-fast, low-cost, and green regeneration of graphite anode using flash joule heating method. *EcoMat.* 2022;4(5):e12212.
- Yuwen C, Liu B, Zhang H, et al. Efficient recovery and regeneration of waste graphite through microwave stripping from spent batteries anode for high-performance lithium-ion batteries. *J Clean Prod.* 2022;333:130197.
- Fan W, Zhang J, Ma R, Chen Y, Wang C. Regeneration of graphite anode from spent lithium-ion batteries via microwave calcination. *J Electroanal Chem.* 2022;908:116087.
- Chen Q, Huang L, Liu J, Luo Y, Chen Y. A new approach to regenerate high-performance graphite from spent lithium-ion batteries. *Carbon.* 2022;189:293-304.
- Kim S, Bang J, Yoo J, et al. A comprehensive review on the pretreatment process in lithium-ion battery recycling. *J Clean Prod.* 2021;294:126329.
- Wang C, Liu M, Thijs M, Ooms FGB, Ganapathy S, Wagemaker M. High dielectric barium titanate porous scaffold for efficient Li metal cycling in anode-free cells. *Nat Commun.* 2021;12:6536.
- Zhang N, Deng W, Xu Z, Wang X. Upcycling of spent LiCoO₂ cathodes via nickel-and manganese-doping. *Carbon Energy.* 2023;5(1):e231.
- Chen W, Salvatierra RV, Li JT, et al. Flash recycling of graphite anodes. *Adv Mater.* 2023;35(8):2207303.
- Yao Y, Huang Z, Hughes LA, et al. Extreme mixing in nanoscale transition metal alloys. *Matter.* 2021;4(7):2340-2353.
- Yao Y, Huang Z, Xie P, et al. High temperature shockwave stabilized single atoms. *Nat Nanotechnol.* 2019;14(9):851-857.

35. Yao Y, Huang Z, Xie P, et al. Carbothermal shock synthesis of high-entropy-alloy nanoparticles. *Science*. 2018;359(6383):1489-1494.
36. Xing Z, Gao N, Qi Y, Ji X, Liu H. Influence of enhanced carbon crystallinity of nanoporous graphite on the cathode performance of microbial fuel cells. *Carbon*. 2017;115:271-278.
37. Bychko I, Abakumov A, Didenko O, Chen M, Tang J, Strizhak P. Differences in the structure and functionalities of graphene oxide and reduced graphene oxide obtained from graphite with various degrees of graphitization. *J Phys Chem Solids*. 2022;164:110614.
38. Wang X, Chen J, Dong C, Wang D, Mao Z. Hard carbon derived from graphite anode by mechanochemistry and the enhanced lithium-ion storage performance. *ChemElectroChem*. 2022;9(5):e202101613.
39. Or T, Gourley SWD, Kaliyappan K, Yu A, Chen Z. Recycling of mixed cathode lithium-ion batteries for electric vehicles: current status and future outlook. *Carbon Energy*. 2020;2(1):6-43.
40. Yi C, Ge P, Wu X, Sun W, Yang Y. Tailoring carbon chains for repairing graphite from spent lithium-ion battery toward closed-circuit recycling. *J Energy Chem*. 2022;72:97-107.
41. Liu B, Huang P, Liu M, Xie Z. Utilization of impurities and carbon defects in natural microcrystalline graphite to prepare silicon-graphite composite anode for high-performance lithium-ion batteries. *J Mater Sci*. 2021;56(31):17682-17693.
42. Yao Y, Huang Z, Li T, et al. High-throughput, combinatorial synthesis of multimetallic nanoclusters. *Proc Natl Acad Sci U S A*. 2020;117(12):6316-6322.
43. Perdew JP, Burke K, Ernzerhof M. Generalized gradient approximation made simple. *Phys Rev Lett*. 1996;77(18):3865-3868.
44. Segall MD, Lindan PJD, Probert MJ, et al. First-principles simulation: ideas, illustrations and the CASTEP code. *J Phys Condens Matter*. 2002;14(11):2717-2744.
45. Banhart F, Kotakoski J, Krashennnikov AV. Structural defects in graphene. *ACS Nano*. 2011;5(1):26-41.
46. Gao W, Mueller JE, Anton J, Jiang Q, Jacob T. Nickel cluster growth on defect sites of graphene: a computational study. *Angew Chem Int Ed*. 2013;52(52):14237-14241.
47. Han Y-C, Liu M-L, Sun L, et al. A general strategy for overcoming the trade-off between ultrasmall size and high loading of MOF-derived metal nanoparticles by millisecond pyrolysis. *Nano Energy*. 2022;97:107125.
48. Ying H, Han W-Q. Metallic Sn-based anode materials: application in high-performance lithium-ion and sodium-ion batteries. *Adv Sci*. 2017;4(11):1700298.
49. Yu L, Zeng K, Li C, et al. High-entropy alloy catalysts: from bulk to nano toward highly efficient carbon and nitrogen catalysis. *Carbon Energy*. 2022;4(5):731-761.
50. Cheng Y, Huang J, Qi H, et al. Controlling the Sn-C bonds content in SnO₂@ CNTs composite to form in situ pulverized structure for enhanced electrochemical kinetics. *Nanoscale*. 2017;9(47):18681-18689.
51. Liang S, Cheng Y-J, Zhu J, Xia Y, Müller-Buschbaum P. A chronicle review of nonsilicon (Sn, Sb, Ge)-based lithium/sodium-ion battery alloying anodes. *Small Methods*. 2020;4(8):2000218.
52. Li W, Sun X, Yu Y. Si-, Ge-, Sn-based anode materials for lithium-ion batteries: from structure design to electrochemical performance. *Small Methods*. 2017;1(3):1600037.
53. Luo J, Zhang J, Guo Z, et al. Recycle spent graphite to defect-engineered, high-power graphite anode. *Nano Res*. 2023;16(4):4240-4245.
54. Khosla N, Narayan J, Narayan R, Sun X-G, Paranthaman MP. Microstructure and defect engineering of graphite anodes by pulsed laser annealing for enhanced performance of lithium-ion batteries. *Carbon*. 2023;205:214-225.
55. Zhang Y, Tao L, Xie C, et al. Defect engineering on electrode materials for rechargeable batteries. *Adv Mater*. 2020;32(7):1905923.
56. Zheng F, Yang Y, Chen Q. High lithium anodic performance of highly nitrogen-doped porous carbon prepared from a metal-organic framework. *Nat Commun*. 2014;5:5261.
57. Dong J, Xue Y, Zhang C, et al. Improved Li⁺ storage through homogeneous N-doping within highly branched tubular graphitic foam. *Adv Mater*. 2017;29(6):1603692.
58. Kim J, Nithya Jeghan SM, Lee G. Superior fast-charging capability of graphite anode via facile surface treatment for lithium-ion batteries. *Microporous Mesoporous Mater*. 2020;305:110325.
59. Wang C, Li Y, Chui Y-S, Wu Q-H, Chen X, Zhang W. Three-dimensional Sn-graphene anode for high-performance lithium-ion batteries. *Nanoscale*. 2013;5(21):10599-10604.
60. Wang M, Wang J, Xiao J, et al. Introducing a pseudocapacitive lithium storage mechanism into graphite by defect engineering for fast-charging lithium-ion batteries. *ACS Appl Mater Interfaces*. 2022;14(14):16279-16288.
61. Han M, Liu G, Jiang J, et al. Realizing spherical lithium deposition by in situ formation of a Li₂S/Li-Sn alloy mixed layer on carbon paper for stable and safe Li metal anodes. *ACS Appl Mater Interfaces*. 2021;13(41):48828-48837.
62. Lu J, Liu S, Liu J, et al. Millisecond conversion of photovoltaic silicon waste to binder-free high silicon content nanowires electrodes. *Adv Energy Mater*. 2021;11(40):2102103.
63. Zhao L-F, Hu Z, Lai W-H, et al. Hard carbon anodes: fundamental understanding and commercial perspectives for Na-Ion batteries beyond Li-ion and K-ion counterparts. *Adv Energy Mater*. 2021;11(1):2002704.
64. Liu Y, Xue JS, Zheng T, Dahn JR. Mechanism of lithium insertion in hard carbons prepared by pyrolysis of epoxy resins. *Carbon*. 1996;34(2):193-200.
65. Qin J, He C, Zhao N, et al. Graphene networks anchored with Sn@ graphene as lithium ion battery anode. *ACS Nano*. 2014;8(2):1728-1738.
66. Derrien G, Hassoun J, Panero S, Scrosati B. Nanostructured Sn-C composite as an advanced anode material in high-performance lithium-ion batteries. *Adv Mater*. 2007;19(17):2336-2340.
67. Qing J, Lekakh S, Xu M, Field D. Formation of complex nuclei in graphite nodules of cast iron. *Carbon*. 2021;171:276-288.
68. Zhang H, Ji Y, Yao Y, et al. Transient and dry recycling of battery materials with negligible carbon footprint and roll-to-roll scalability. *Energy Environ Sci*. 2023;16(6):2561-2571.

69. Wang J, Ma J, Jia K, et al. Efficient extraction of lithium from anode for direct regeneration of cathode materials of spent Li-ion batteries. *ACS Energy Lett.* 2022;7(8):2816-2824.
70. Lu J, Zhao Y, Kang Y, et al. Surplus energy utilization of spent lithium-ion batteries for high-profit organolithiums. *Carbon Energy.* 2023;5(6):1-10.
71. Yang Y, Song S, Lei S, et al. A process for combination of recycling lithium and regenerating graphite from spent lithium-ion battery. *Waste Manage.* 2019;85:529-537.
72. Thompson DL, Hartley JM, Lambert SM, et al. The importance of design in lithium ion battery recycling—a critical review. *Green Chem.* 2020;22(22):7585-7603.

SUPPORTING INFORMATION

Additional supporting information can be found online in the Supporting Information section at the end of this article.

How to cite this article: Cheng Z, Luo Z, Zhang H, et al. Targeted regeneration and upcycling of spent graphite by defect-driven tin nucleation. *Carbon Energy.* 2023;e395. doi:10.1002/cey2.395